HHS Public Access

Author manuscript

Nucl Med Biol. Author manuscript; available in PMC 2020 July 22.

Published in final edited form as:

Nucl Med Biol. 2020 ; 80-81: 1–12. doi:10.1016/j.nucmedbio.2019.11.002.

Multimodality labeling strategies for the investigation of nanocrystalline cellulose biodistribution in a mouse model of breast cancer

Mirkka Sarparanta[a,d,*], **Jacob Pourat**[a,1], **Kathryn E. Carnazza**[a,1], **Jun Tang**[a], **Navid Paknejad**[c], **Thomas Reiner**[a,f], **Mauri A. Kostiainen**[e], **Jason S. Lewis**[a,b,f,g]

[a]Department of Radiology, Memorial Sloan Kettering Cancer Center, New York, NY, USA [b]Program in Molecular Pharmacology, Memorial Sloan Kettering Cancer Center, New York, NY, USA [c]Molecular Cytology Core Facility, Memorial Sloan Kettering Cancer Center, New York, NY, USA [d]Department of Chemistry, Radiochemistry, University of Helsinki, Helsinki, Finland [e]Biohybrid Materials Group, Department of Bioproducts and Biosystems, Aalto University, Espoo, Finland [f]Department of Radiology, Weill Cornell Medical College, New York, NY, USA [g]Department of Pharmacology, Weill Cornell Medical College, New York, NY, USA

Abstract

Methods—We have developed a nuclear and fluorescence labeling strategy for nanocrystalline cellulose (CNC), an emerging biomaterial with versatile chemistry and facile preparation from renewable sources. We modified CNC through 1,1′-carbonyldiimidazole (CDI) activation with radiometal chelators desferrioxamine B and 1,4,7-triazacyclononane-1,4,7-triacetic acid (NOTA), allowing for the labeling with zirconium-89 ($t_{1/2}$ = 78.41 h) and copper-64 ($t_{1/2}$ = 12.70 h), respectively, for non-invasive positron emission tomography (PET) imaging. The far-red fluorescent dye Cy5 was added for *ex vivo* optical imaging, microscopy and flow cytometry. The multimodal CNC were evaluated in the syngeneic orthotopic 4T1 tumor model of human stage IV breast cancer.

Results—Modified CNC exhibited low cytotoxicity in RAW 264.7 macrophages over 96 h, and high radiolabel stability *in vitro*. After systemic administration, radiolabeled CNC were rapidly sequestered to the organs of the reticulo-endothelial system (RES), indicating immune recognition and no passive tumor targeting by the enhanced permeability and retention (EPR) effect. Modification with NOTA was a more favorable strategy in terms of radiolabeling yield, specific radioactivity, and both the radiolabel and dispersion stability in physiological conditions. Flow

*Corresponding author at: Department of Chemistry, Radiochemistry, P.O. Box 55, A.I. Virtasen aukio 1, FI-00014, University of Helsinki, Finland., mirkka.sarparanta@helsinki.fi (M. Sarparanta).

[1]These authors contributed equally

Declaration of competing interest

The authors have no conflicts of interest to disclose.

Appendix A. Supplementary data

Supplementary Figs. S1 through S9, and detailed experimental methods for the 4T1 allograft surgery, the BT-474 tumor model, whole blood fractionation and flow cytometry. Supplementary data to this article can be found online at https://doi.org/10.1016/j.nucmedbio.2019.11.002.

cytometry analysis of Cy5-positive immune cells from the spleen and tumor corroborated the uptake of CNC to phagocytic cells.

Conclusions—Future studies on the *in vivo* behavior of CNC should be concentrated on improving the nanomaterial stability and circulation half-life under physiological conditions and optimizing further the labeling yields for the multimodality imaging strategy presented.

Advances in knowledge—Our studies constitute one of the first accounts of a multimodality nuclear and fluorescent probe for the evaluation of CNC biodistribution *in vivo* and outline the pitfalls in radiometal labeling strategies for future evaluation of targeted CNC-based drug delivery systems.

Implications for patient care—Quantitative and sensitive molecular imaging methods provide information on the structure–activity relationships of the nanomaterial and guide the translation from *in vitro* models to clinically relevant animal models.

Keywords

Nanocrystalline cellulose; Biodistribution; Multimodality; Labeling; Imaging; Positron emission tomography (PET)

1. Introduction

Nanoscale drug delivery systems are being intensely investigated for targeted delivery of chemotherapeutic agents to tumors with the potential advantages of concentrating the active pharmaceutical at the tumor by the enhanced permeability and retention (EPR) effect, protecting sensitive payloads from premature release and degradation, limiting off-target toxicity, and providing sustained release at the tumor [1–4]. Despite the great potential, many nanoscale drug delivery systems fall short of the anticipated therapeutic potential *in vivo* because of limitations due to residence time in circulation, aggregation, accumulation to non-target organs, and poor penetration to the tumor tissue [5]. Sensitive and quantitative molecular imaging techniques are valuable tools for the initial *in vivo* evaluation of nanoscale drug delivery systems in preclinical models as they allow the tracking of the nanosystem behavior non-invasively in real time with minimal disturbance to the sequestration of the nanomaterial and payload release [6]. The hallmark of nuclear molecular imaging techniques, positron emission tomography (PET) and single-photon emission computed tomography (SPECT) is their exceptional sensitivity arising from the unlimited penetration of gamma irradiation in tissues. However, multimodality probe constructs where the radiolabel is combined with a fluorescent label offer the additional advantage of studying these interactions with the same probe in cells and tissues with fluorescence microscopy and optical imaging [7,8].

Nanocrystalline cellulose is a top-down nanomaterial prepared from various renewable sources including wood pulp, bamboo, cotton, bacteria and tunicate mantles by preferential acid hydrolysis of disordered amorphous regions in the biopolymer [9,10]. The physicochemical properties of the cellulose nanomaterials such as size, shape, and surface functionality, can be controlled by the utilization of various mineral acids and sources of cellulose [11,12], which makes nanocrystalline cellulose a versatile platform for drug

delivery. Nanoscale cellulose materials are classified according to material dimensions either as nanofibrils (NFC, 4–20 nm in diameter, 500–2000 nm in length), or nanocrystals or whiskers (CNC, 3–5 nm, 50–500 nm) [13]. An important distinction between nanofibrillar and nanocrystalline cellulose is that NFC contains both crystalline and amorphous regions, whereas the number of the latter are significantly reduced in CNC resulting in high order of crystallinity of the material. The crystallinity translates to high tensile strength and rigidity of CNC compared to NFC and many other nanomaterials explored for drug delivery. Several aspects of CNC make it an appealing candidate material for drug delivery applications. First, the as-hydrolyzed surface of CNC is negatively charged facilitating efficient loading of both charged and non-ionized payloads, or upon modification with cetrimonium bromide (CTAB), hydrophobic anticancer drugs [14]. Second, the abundant −OH termination of the CNC surface provides an easily accessible handle for further chemical surface modification. The principal strategies to modify CNC surface chemistry include oxidation with TEMPO, activation with 1,1′-carbonyldiimidazole (CDI), cationization *via* epoxide ring opening, and esterification by acid chlorides and anhydrides, reviewed comprehensively by Lam et al. [15].

To date, CNC has been primarily investigated in sustained release matrices including aerogels, films, wound dressings, and in oral formulations [16–18]. Despite increasing interest for drug delivery systems based on CNC scaffolds, only a few reports have investigated the behavior of CNC in preclinical models after systemic administration. This is surprising, as the aspect ratios of cellulose nanocrystals prepared from cotton match those of carbon nanotubes and tobacco mosaic virus (TMV) capsids, both of which have been successfully employed for systemic carrier-mediated drug delivery in animal models of cancer [19–21]. A high aspect ratio has been even shown to promote cellular internalization and tumor penetration of non-targeted rod-shaped nanoparticles over spherical ones [22,23]. Furthermore, CNC has been shown to have a low cytotoxic and genotoxic profile in human monocyte-derived macrophages, bronchial epithelial cells and fibroblasts [24,25], human stem cells [26,27], in embryonic zebrafish [28], and in a single study with Alexa Fluor 633 – labeled CNC in immunocompetent NFR mice [29]. Fluorescent labeling of cellulose nanocrystals with fluorescein isothiocyanate (FITC) and Rhodamine B isothiocyanate (RBITC) has been reported, but applications of these conjugates have been limited to studies in cells [30,31]. Therefore, the material properties seem to be suited for carrier-mediated drug delivery after systemic administration, and further evaluation of CNC behavior *in vivo* is warranted in order to propel the development of targeted drug delivery systems based on nanocrystalline cellulose scaffolds.

Here we describe a multimodality labeling strategy for CNC for evaluation in a preclinical animal model with PET and fluorescence imaging. The cellulose nanocrystals are activated with 1,1′-carbonyldiimidazole (CDI) followed by a single-step conjugation of amino-functionalized chelators desferrioxamine B (DFO) and 1,4,7-triazacyclononane-1,4,7-triacetic acid (NOTA) for positron-emitting radiometals zirconium-89 ($t_{1/2}$ = 78.41 h) and copper-64 ($t_{1/2}$ = 12.70 h), and the fluorophore Cyanine 5 (Scheme 1). The developed imaging probes are characterized for cytotoxicity in murine RAW 264.7 macrophages and evaluated *in vivo* for immune cell specificity and passive tumor targeting in a mouse model of human stage IV breast cancer.

2. Materials and methods

2.1. Materials

All chemicals unless denoted otherwise were purchased from Sigma-Aldrich (St. Louis, MO, USA) and were used without further purification. Cyanine5 (Cy5) amine (95% purity) was from Lumiprobe Corporation (Hallandale Beach, FL, USA), and *p*-NH_2-Bn-NOTA (≥94%) from Macrocyclics (Dallas, TX, USA). Ultrapure water (18.2 MΩ cm^{-1}) was produced on an Elga Purelab Ultra system (Elga LCC, Woodridge, IL, USA). Zirconium-89 was prepared in-house at Memorial Sloan Kettering Cancer Center (MSKCC) on an TR 19/9 variable beam energy cyclotron (Ebco Industries, Richmond, BC, Canada) in a $^{89}Y(p,n)^{89}Zr$ reaction and extracted from the foil using methods reported in literature [32]. This afforded ^{89}Zr as [^{89}Zr]Zr-oxalate at molar activity ranging from 17.76 to 45.14 MBq μmol^{-1}. [^{64}Cu]$CuCl_2$ produced in a $^{64}Ni(p,n)^{64}Cu$ reaction was purchased from Mallinckrodt Institute of Radiology, Washington University, St. Louis, MO, USA. The molar activity for copper-64 used for the studies ranged from 259 to 984 GBq μmol^{-1}. RAW 264.7 and 4T1 cell lines were obtained from ATCC (Manassas, VA, USA). The 4T1-tdTomato cells were a kind gift from the laboratory of Dr. Moritz Kircher, Department of Radiology, MSKCC. All culture media used were supplied by the MSKCC Media Preparation Core Facility.

2.2. Synthesis of multimodal CNCs

Unmodified cellulose nanocrystals were prepared from ashless cotton cellulose filter paper by hydrolysis in sulfuric acid following a literature procedure [33]. In a typical synthesis procedure, 10 mg of CNC was used as the starting material. After activation with 10 mg of 1,1′-carbonyldiimidazole (CDI, 1:1 *w*/w to CNC, 10 mM final concentration) in 6.2 ml of anhydrous dimethyl sulfoxide (DMSO) under inert atmosphere for 22 h at 40 °C, DFO (0.5 mg, 1:20 w/w to CNC, 0.15 mM) or *p*-NH_2-Bn-NOTA (5 mg, 1:2 w/w to CNC, 1.93 mM), and Cy5 amine dye (0.1 mg from 10 mg ml^{-1} solution in DMSO, 1:100 w/w, 30.6 μM) were added, and the reaction mixture in anhydrous DMSO (5 ml) was stirred at 600 rpm under inert atmosphere for 22 h at 40 °C. Modified CNCs were purified with sequential centrifugation and resuspension in DMSO, 1 × PBS, pH = 7.4, and ultrapure water, followed by dialysis for 72 h against ultrapure water. Purified nanocrystals were lyophilized, stored at +4 °C and used as prepared for subsequent experiments.

2.3. Determination of CNC size distribution with atomic force microscopy (AFM)

Size distribution of the synthesized CNC materials was determined with atomic force microscopy (AFM). Briefly, single-nanocrystal suspensions of unmodified CNC, CNC-NOTA-Cy5, and CNC-DFO-Cy5 were prepared by sonication of concentrated (5 mg ml^{-1}) nanocrystal samples in ultrapure water on an ultrasonic probe, followed by sedimentation of aggregates by low-speed centrifugation. The supernatant single nanocrystal suspensions were applied to mica substrates, allowed to attach for a maximum of 15 min and the substrate was subsequently washed with ultrapure water. Images were acquired on MFP-3D-BIO AFM (Asylum Research, Santa Barbara, CA, USA) on an Axio Observer inverted optical microscope (Carl Zeiss Microscopy GmbH, Jena, Germany). For AFM image analysis, the images were exported as specified *Z*-scales from the Asylum Research software (version 14.13.143) into MetaMorph (version 7.8.10, Molecular Devices, Sunnyvale, CA,

USA). A customized script in MetaMorph was used to identify individual nanocrystals for morphometric analysis. Length and width were determined by thresholding whereas the diameter or height of the CNC was considered to be the average of the 20 brightest pixels of each nanocrystal. The journal was set to prompt the user for visual confirmation of the presence of a single crystal in each individual image submitted for analysis.

2.4. Zeta potential measurements

Zeta potential of unmodified and modified cellulose nanocrystals was measured in ultrapure water in a disposable folded capillary cell on a Zetasizer Nano ZS instrument (Malvern Instruments Ltd., Malvern, United Kingdom). The zeta potential distribution was determined from the electrophoretic mobility of the cellulose nanocrystals using the Smoluchovski relation as an average of three measurements.

2.5. Cell culture

All cell lines were maintained in T-75 culture flasks (Corning) in humidified atmosphere at +37 °C and 5% CO_2. RAW 264.7 macrophages were cultured in Dulbecco's Modified Eagle's Medium (DMEM) with 10% fetal bovine serum with 100 units ml^{-1} penicillin G and 100 μg ml^{-1} streptomycin. 4T1 and 4T1-tdTomato cells were cultured either in DMEM or RPMI-1640 media supplemented with 10% fetal bovine serum, 100 units ml^{-1} penicillin G and 100 μg ml^{-1} streptomycin.

2.6. Cytotoxicity and confocal microscopy in murine RAW 264.7 macrophages

The cytotoxicity of the modified CNC probes was determined in RAW 264.7 macrophages using the Molecular Probes LIVE/DEAD® Viability/Cytotoxicity Kit for mammalian cells (Thermo Fisher Scientific, Waltham, MA, USA) according to the manufacturer's instructions. For the assay, RAW 264.7 cells were plated on #1.5 Nunc Lab-Tek II chambered coverglasses (Thermo Fisher Scientific) at a density of 25,000 cells per well in 250 μl of DMEM and allowed to attach overnight. The medium was replaced with 200 μl of medium containing 5, 25, or 100 μg ml^{-1} of unmodified CNC, DFO-CNC-Cy5, or NOTA-CNC-Cy5 and the samples were incubated at +37 °C, 5% CO_2 for 6, 24, and 96 h. After incubation the cells were stained with 2 μM calcein AM (for viable cells) and 4 μM ethidium homodimer-1 (dead cells) in 1 × PBS, pH = 7.4. Saponin (0.1% *w*/w) and medium only were used as controls for dead and viable cells, respectively. The cells were imaged on a Leica TCS SP8 confocal microscope using excitation wavelength 495 nm and emission filters for maxima at 515 nm (calcein AM) and 635 nm (EthD-1 in the presence of DNA). Images were obtained at 40× magnification and 0.75 zoom, and snapshots rendering ≥100 cells for analysis (typically from 4 to 6 sites on the well) were recorded. The proportion of live and dead cells was determined using MetaMorph software.

2.7. Radiolabeling of multimodal CNCs with ^{89}Zr and ^{64}Cu

All solutions used for radiolabeling were prepared from trace metal-free salts in ultrapure water rendered trace metal-free by treatment with Chelex 100 resin (Bio-Rad Laboratories, Hercules, CA, USA) at a concentration of 5.0 g l^{-1} for 12 h. For radiolabeling with ^{89}Zr, 0.75–0.9 mg of DFO-CNC-Cy5 nanocrystals were dispersed in 2.5 ml of Chelex-treated

ultrapure water with sonication on an ultrasonic probe, and the volume supplemented to 5 ml with 0.2 M ammonium acetate, pH = 7.0, to give final concentration of 0.1 M ammonium acetate. [^{89}Zr]Zr-oxalate (64.4 ± 11.8 MBq) was neutralized with 1 M Na_2CO_3 solution, and added to the nanocrystals. The mixture was vigorously shaken on a vortex shaker protected from light at ambient temperature for 12 h. The [^{89}Zr]Zr-DFO-CNC-Cy5 was separated from unreacted radiolabel by sequential washes in 1 ml of 1 mM DTPA, ultrapure water and 1 × PBS, pH = 7.4 before final formulation to 0.5% Kolliphor HS 15–1 × PBS, pH = 7.4 by sonication. The nanocrystals were pelleted by centrifugation at 10,000 rpm for 10 min between washes, and the radioactivity remaining in the nanocrystal pellet and the supernatant was measured after each wash on a dose calibrator (Capintec Inc., Florham Park, NJ, USA). The radiochemical purity of the product was determined by paper chromatography on an iTLC-SA strip (Agilent Technologies Inc., Santa Clara, CA, USA) eluted with 50 mM DTPA. The strip was scanned on Bioscan AR-2000 radio-TLC scanner (Eckert & Ziegler Radiopharma Inc., Hopkinton, MA, USA). For radiolabeling with ^{64}Cu, 0.5–1.2 mg NOTA-CNC-Cy5 nanocrystals were dispersed in 1 ml of 0.1 M ammonium acetate, pH = 4.0 by sonication on an ultrasonic probe, and 68.8 ± 23.7 MBq [^{64}Cu]$CuCl_2$ was added. The reaction was stirred (750 rpm) at 80 °C for 20 min, and the nanocrystals purified and formulated as described for the [^{89}Zr]Zr-DFO-CNC-Cy5. Radiochemical purity was determined on an iTLC-SG strip (Agilent Technologies) eluted with 50 mM ethylenediaminetetraacetic acid (EDTA), and analyzed as described above. Radiolabel stability *in vitro* was determined using the iTLC methods described above after incubation of the radiolabeled CNC in 50% human serum–1 × PBS, pH = 7.4 at +37 °C with shaking at 500 rpm.

2.8. 4T1 orthotopic mammary carcinoma model

Allografts of 1 × 10^6 4T1 or 4T1-tdTomato cells in 50 μl of culture medium were inoculated into surgically exposed right mammary fat pad of 6–10 week-old female Balb/c mice (Charles River Laboratories, Kingston, NY, USA) under isoflurane anesthesia. All experiments were commenced on day 9 following tumor implantation, when the tumors had reached an average diameter of 8 mm in the largest dimension. All animal experiments were conducted under the ethical approval of the Institutional Animal Care and Use Committee of Memorial Sloan Kettering Cancer Center, or under the project license granted by the National Board for Animal Experimentation in Finland in compliance with the respective federal and European regulations and guidelines. Detailed descriptions of the surgical method, the fractionation of whole mouse blood for radioactivity counting, and the generation of the positive control tissue (BT-474 model) for the anti-Cy5 immunohistochemistry are given in the Supplementary Information.

2.9. Biodistribution and blood half-life determination in orthotopic 4T1 allograft-bearing mice

4T1 allograft-bearing mice were injected intravenously with either ^{89}Zr-labeled DFO-CNC-Cy5 or ^{64}Cu-labeled NOTA-CNC-Cy5 nanocrystals in 200 μl of 0.5% Kolliphor HS 15–1 × PBS, pH = 7.4 in the lateral tail vein. For an *ex vivo* biodistribution study, a dose of either 1.85 MBq (30 μg) of [^{89}Zr]Zr-DFO-CNC-Cy5 or 3.7 MBq (30 μg) of [^{64}Cu] Cu-NOTA-CNC-Cy5 was used. Animals were sacrificed by CO_2 asphyxiation followed by cervical

dislocation at the designated time points, and tissues were collected for radioactivity measurements. The samples were measured on a Wizard 3″ automated gamma counter (PerkinElmer, Waltham, MA, USA) for 60 s. Additionally, a subset of animals was imaged under isoflurane anesthesia on Focus 120 Micro-PET small animal PET scanner (Siemens Medical Solutions, Malvern, PA, USA) at designated time points after nanocrystal administration to visualize CNC biodistribution in the same animal subject as a function of time. For the longitudinal imaging experiment, higher doses of 3.7 MBq (60 μg) of [^{89}Zr]Zr-DFO-CNC-Cy5 and 7.4 MBq (60 μg) of [^{64}Cu]Cu-NOTA-CNC-Cy5 were used to permit registration of at least 20 million coincidence events. Imaging data was processed on ASIPro software (Concord Biosystems). Blood half-life for [^{89}Zr]Zr-DFO-CNC-Cy5 and [^{64}Cu]Cu-NOTA-CNC-Cy5 was determined after single intravenous injection of the radiolabeled nanocrystals. Venous blood samples were collected at 5, 15, 30, 60, 120, and 240 min following administration either into a pre-weighed microhematocrit capillary through a temporary cannula in the tail vein contralateral to the injection site, or by cardiac puncture after CO_2 asphyxiation. The radioactivity in the blood samples was measured on an automated gamma counter.

2.10. Ex vivo fluorescence imaging and histology

For determination of the biodistribution based on the Cy5 fluorescence label, 4T1 allograft-bearing mice maintained on a low-autofluorescent diet (Teklad 16% protein rodent diet, Envigo RMS, Indianapolis, IN, USA) were intravenously injected with 25 μg of nonradioactive DFO-CNC-Cy5 or NOTA-CNC-Cy5. A control mouse received the same amount of unmodified, non-fluorescent CNC. The mice were sacrificed 24 h post-injection and the principal tissues that had showed uptake of radiolabeled CNC were removed and imaged individually on IVIS Spectrum optical imaging system (PerkinElmer, Waltham, MA, USA) under epifluoresence illumination in the spectral unmixing mode. Tissue autofluorescence spectra were determined from the corresponding tissues from an animal injected with the unmodified CNC. Fluorescence images were recorded and analyzed using the Living Image software (version 4.6, PerkinElmer). After imaging the tissues were processed for cryosectioning for fluorescence microscopy and automated hematoxylin–eosin (H&E) staining, or fixed in 10% neutral buffered formalin and processed for paraffin sections. The paraffin sections were stained in an automated system with a mouse monoclonal anti-Cy5 antibody at a concentration of 7.5 μg ml^{-1} followed by 3,3′-diaminobenzidine (DAB) staining and counterstaining with hematoxylin. Cryosections (for fluorescence) were post-fixed with 4% paraformaldehyde in 1 × PBS, pH = 7.4, counterstained with 1:1000 DAPI (4′,6-diamidino-2-phenylindole), and imaged on a Zeiss AxioPlan 2 widefield fluorescence microscope using excitation and emission settings for DAPI, and Alexa Fluor 647, respectively. H&E -stained sections were imaged on the same system under brightfield illumination. Anti-Cy5 -stained slides were scanned on an automated slide scanner (3DHistech Mirax Pannoramic) and processed on the Pannoramic Viewer software. Detailed description of the generation of the Cy5-trastuzumab-labeled BT-474 positive control tissue for anti-Cy5 antibody staining is described in the Supplementary Information.

2.11. Isolation of phagocytic cells and flow cytometry analysis

For flow cytometry analysis of CNC uptake to phagocytic immune cells, mice bearing orthotopic 4T1-tdTomato mammary fat pad allografts were administered with 50 μg of DFO-CNC-Cy5 and NOTA-CNC-Cy5 in 200 μl of 0.5% Kolliphor HS 15–1 × PBS, pH = 7.4 or vehicle intravenously. At 120 min after administration, the mice were sacrificed by CO_2 asphyxiation and perfused transcardially with ice-cold 100 units ml^{-1} heparin solution in 1 × PBS, and the tumor and spleen were collected. Minced tissues (200 mg for tumor and 100 mg for spleen) were digested with a cocktail containing 4 units ml^{-1} liberase TH, 40 units ml^{-1} hyaluronidase, and 40 units ml^{-1} DNAse at 37 °C for 30 min (spleen) and 60 min (tumor). The cell suspension was filtered through a 70-μm cell strainer and the cells were collected by centrifugation at 400 *g* at 4 °C for 5 min. The red blood cells in the spleen sample were removed by a treatment with red blood cell lysis buffer (BD Biosciences, San Jose, CA, USA). The cell number in the suspensions was determined on an automated cell counter (Vi-CELL, Beckman Coulter, La Brea, CA, USA) and the concentration adjusted to 10×10^6 cells ml^{-1}. Aliquots of 2×10^6 cells per sample were stained with the appropriate antibodies (see Supplementary Information for dilutions and respective fluorescent labels) and DAPI and analyzed on a BD LSR Fortessa flow cytometry analyzer.

2.12. Statistical analysis

Where applicable, statistical significance between groups was determined using GraphPad Prism (version 6.0f, GraphPad Software Inc., La Jolla, CA, USA). The statistical methods used are denoted for each data set in the Results and Discussion section.

3. Results and discussion

3.1. Preparation and characterization of multimodal CNC imaging probes

Several strategies, including TEMPO oxidation [34], amidation [35] and hydrazone conjugation to the reducing end aldehyde [29,36] could be employed for the chemical modification of CNC for radiolabeling. In this study, activation of the hydroxyl-terminated surface with CDI afforded a straight-forward strategy for the conjugation of desferrioxamine B (DFO), *p*-NH_2-benzyl-NOTA, and Cy5-amine to the CNC surface, in line with the previous observation that the stability of the reducing end hydrazone linkage is compromised in the acidic radiolabeling conditions needed for radiometal chelation [36]. The constructs are named DFO-CNC-Cy5 and NOTA-CNC-Cy5. The amount of DFO and NOTA chelators needed for sufficient radiolabeling yield with ^{89}Zr and ^{64}Cu, respectively, was determined with pilot radiolabeling experiments and was shown to be 20 equivalents to the nanocrystal mass for DFO and 2 equivalents for *p*-NH_2-benzyl-NOTA. This afforded decay-corrected radiochemical yields (RCY) of 61 ± 16% ($n = 5$) and 65 ± 3% ($n = 5$) for ^{89}Zr and ^{64}Cu, respectively. The maximum specific activity attained was 59.2 MBq mg^{-1} for [^{89}Zr]Zr-DFO-CNC-Cy5 and 96.2 MBq mg^{-1} for [^{64}Cu]Cu-NOTA-CNC-Cy5, with radiochemical purity exceeding 99% for both radiolabeled constructs after the purification (determined by radio-iTLC).

Quantitative RCY could not be attained for either isotope in this experimental setup likely because of the transient adsorption of the radiometals to the CNC surface. The presence of

this phenomenon was corroborated by the removal of surface-bound radiolabel with subsequent washing with 50 mM diethylenetriamine pentaacetic acid (DTPA), and the lack of stable radiolabeling in unmodified as-hydrolyzed CNC (data not shown). Radiolabel stability in human serum was high over the time course of an *in vivo* experiment, 95.1 ± 1.2% of radiolabel remaining in nanocrystals for [^{89}Zr]Zr-DFO-CNC-Cy5 after 7 days of incubation at 37 °C (Supplementary Fig. S1a), and 94.4 ± 2.3% for [^{64}Cu]Cu-NOTA-CNC-Cy5 at 24 h (Supplementary Fig. S1b).

A 1:100 (*w*/w) ratio of Cy5-amine to CNC resulted in a fluorescent product. The scattering and bright fluorescence of the CNC products rendered the material unsuitable for particle size determination using dynamic light scattering (DLS), and nanocrystal size was instead determined with atomic force microscopy (AFM) using an automated journal in the MetaMorph software to measure the dimensions of individual nanocrystals. Size distributions for unmodified CNC, DFO-CNC-Cy5, and NOTA-CNC-Cy5 with representative AFM images are presented in Fig. 1. A considerably smaller number of CNC could be measured for DFO-CNC-Cy5 than for unmodified and NOTA-modified nanocrystals because of prominent aggregation of the nanomaterial upon application onto the mica substrate. Surface modification of single-crystal suspensions of CNC can be challenging as the aqueous suspension is often stabilized by the residual sulfate ester groups (from the hydrolysis with sulfuric acid) on the CNC surface [37]. Subsequent chemical modifications may result in destruction or masking of the sulfate residues, and consequently, reduce the hydrophilicity of the nanomaterial. This was especially true for the case of DFO, the conjugation of which to the CNC surface resulted in pronounced loss in the stability of the CNC suspension in aqueous and physiological media including phosphate-buffered saline (PBS) and serum at concentrations exceeding 1 mg ml^{-1}. The aggregation of DFO-CNC-Cy5 is possibly a result of the ability of the DFO structure to promote hydrogen-bonding between adjacent DFO chains, a phenomenon that has been previously described for DFO-containing monolayers for iron sensor applications [38], and for the self-assembly of bacterial vesicles upon sequestration of iron [39]. In order to stabilize the nanocrystals for systemic administration, we chose to use 0.5% Kolliphor® HS 15, a non-ionic solubilizer in the final formulation. Kolliphor® has been previously reported to improve the dispersion of hydrophobic porous silicon nanoparticles at physiological salt concentration and is safe for intravenous administration in rodents [40]. Characterization data for the CNC used in this study are compiled in Table 1.

3.2. Modified CNC exhibit low cytotoxicity in murine RAW 264.7 macrophages

Cytotoxicity of the modified CNC was investigated in murine RAW 264.7 macrophages, a widely used cell model to study cytotoxic effects of engineered nanomaterials. Luminescence and fluorescence –based 96-well-plate assays were quickly found to be incompatible with Cy5-labeled CNC because of scattering and strong adsorption of the reagents to the CNC in culture resulting in readouts higher than for the positive control. In order to overcome this problem, we chose to use the LIVE/DEAD® Cell Viability Assay (Molecular Probes, Thermo Fisher Scientific) with confocal microscopy to obviate the issue with scattering and nanocrystal aggregation. The assay is based on the fluorescence detection of two reagents, ethidium homodimer (EthD-1) staining DNA after loss of plasma

membrane integrity in dead cells, and Calcein AM converted to bright fluorescent product by intracellular esterase activity in viable cells. Cell viability after incubation with sterilized unmodified CNC, NOTA-CNC-Cy5, and DFO-CNC-Cy5 was determined after 6, 24, and 96 h, extending over one doubling time of the cell line. Saponin (0.1%) in medium and nanocrystal-free medium was used as controls for dead and viable cells, respectively. Representative microscopy images at 96 h are shown in Fig. 2a, with quantification of the results at each time point in Fig. 2b–d. Representative confocal microscopy images for the earlier time points can be found in Supplementary Fig. S2a–S2b. At the 6 h time point, the viability of RAW 264.7 cells incubated with NOTA and DFO modified CNC was reduced compared to the positive control, while no difference was seen for the unmodified CNC. At 24 h, the viability was lower for unmodified CNC, and the highest 100 μg/mL concentration of NOTA-CNC-Cy5, but no difference was seen for DFO-CNC-Cy5 at this time point. After 96 h, only slight reduction in viability was seen at the highest concentration for both NOTA-CNC-Cy5 and DFO-CNC-Cy5, while no statistically significant differences were observed for unmodified CNC or lower concentrations of the modified CNC when compared to the control for viable cells. The morphology of the RAW 264.7 incubated with NOTA-CNC-Cy5 and DFO-CNC-Cy5 appears to change at the 96 h towards a phenotype of enlarged cells with increased number of cytoplasmic vacuoles possibly indicative of nanomaterial internalization and inflammatory response [41–43].

Multimodal CNC show transient lung uptake and rapid sequestration to the RES in syngeneic mouse model of breast cancer.

Surgical orthotopic implantation of murine 4T1 mammary adenocarcinoma cells to the mammary fat pad of Balb/c mice recapitulates the progression of human breast cancer with metastasis [44]. The orthotopic 4T1 model has become widely used in nanomaterial studies because of the ability to conduct studies in immunocompetent animals, the high take rate and rapid growth of the allograft, spontaneous metastasis, and pronounced EPR effect allowing passive tumor targeting [45]. After intravenous administration to tumor-bearing mice, both [^{89}Zr]Zr-DFO-CNC-Cy5 and [^{64}Cu]Cu-NOTA-CNC-Cy5 showed rapid accumulation from circulation to the principal organs of the reticuloendothelial system (RES), the liver and the spleen, in the PET images with minimal tumor uptake (Fig. 3a–b), suggesting that the circulation residence time of CNC is not optimal to permit passive tumor accumulation. *Ex vivo* biodistribution at 24 h showed significant differences for CNC accumulation in the blood, tumor, spleen, pancreas, liver, lung and bone for the two nanocrystal constructs (Fig. 3c). Biodistribution data for earlier time points is presented in Supplementary Fig. S3a–b for [^{64}Cu]Cu-NOTA-CNC-Cy5 and Supplementary Fig. S4a for [^{89}Zr]Zr-DFO-CNC-Cy5.

The sequestration of [^{64}Cu]Cu-NOTA-CNC-Cy5 from the circulation to the liver and spleen was extremely rapid, with radioactivity in the blood dropping to <1% of the injected dose per gram (ID%/g) within 1 h of nanocrystal administration. Maximum tumor-to-blood ratio of 2.20 ± 0.33 was attained at 4 h post-injection (p.i.) as shown in Supplementary Fig. S3c. For [^{89}Zr]Zr-DFO-CNC-Cy5, clearance from the circulation was markedly slower, and tumor-to-blood ratio peaked at the last time point of the biodistribution study, 48 h p.i., reaching 5.71 ± 1.33 (Supplementary Fig. S4b). The lung uptake of both materials was

initially high, but cleared over time, possibly indicating trapping of the nanocrystals upon injection and subsequent removal by phagocytosis to patrolling immune cells in the circulation [46,47]. Proportion of CNC ending up to the liver *versus* the spleen was different for [^{89}Zr] Zr-DFO-CNC-Cy5 and [^{64}Cu]Cu-NOTA-CNC-Cy5, likely arising from the differences in the physicochemical properties of the two materials and their impact on the subsequent formation of the plasma protein corona *in vivo* [48–50]. Splenic uptake was significantly lower for [^{89}Zr]Zr-DFO-CNC-Cy5, possibly an indication that the DFO-modified nanocrystals resist physical filtration in the interendothelial slits – the fenestrations between the venous sinus and the red pulp – in the spleen [51].

The blood half-life of both nanomaterials was determined by radioactivity measurement of venous blood samples collected at 5, 15, 30, 60, 120, and 240 min after nanomaterial administration. As expected, the blood half-life of [^{64}Cu]Cu-NOTA-CNC-Cy5 was extremely short, mere 4.0 ± 3.1 min (Fig. 4a), in accordance with the rapid clearance of the material to the lung and liver from the circulation seen in the biodistribution study. For [^{89}Zr]Zr-DFO-CNC-Cy5 the situation was much more curious, as the initial blood half-life curve showed a rising phase indicative of the sustained release of a radiolabeled species to the circulation likely from the lung (Fig. 4b), where about 40% of the injected dose remained at 2 h p.i. according to the biodistribution results (Supplementary Fig. S4a). The blood half-life of the released zirconium-89 species was determined from venous blood samples supplemented with the blood samples collected by cardiac puncture at later points in the biodistribution study and gave a value of 4.24 ± 2.22 h (Fig. 4c).

Several studies with [^{89}Zr]Zr-DFO-radioimmunoconjugates have shown that the long-term *in vivo* stability of the DFO chelator for ^{89}Zr is not infinite [52–54]. Released ^{89}Zr has been shown to accumulate in the skeleton [55,56], and increased uptake at 24 h and 48 h p.i. of [^{89}Zr]Zr-DFO-CNC-Cy5 in bone were also seen in this study. Consequently, the bone tropism of CNC reported earlier by Colombo et al. [29] could not be corroborated in our study, as the [^{64}Cu]Cu-NOTA-CNC-Cy5 particles showed only minimal bone uptake. The released ^{89}Zr could also be bound to endogenous plasma proteins, perturbing the intended biodistribution. As a control to determine the *in vivo* radiolabel stability, 4T1 tumor-bearing mice were administered with 1.85 MBq of [^{89}Zr]Zr-oxalate in physiological saline intravenously and sacrificed at the same time points as for the [^{89}Zr]Zr-DFO-CNC-Cy5 study (Supplementary Fig. S5a–c). At 2 h p.i., significantly higher amount of radioactivity was seen in the blood for the [^{89}Zr]Zr-oxalate group, and in the lung for the nanocrystal-receiving animals (Supplementary Fig. S5a). At 24 h, the radioactivity remaining in blood was similar for both of the groups, but significantly higher ID %/g was seen in the tumor and bone for the [^{89}Zr]Zr-oxalate group, whereas the uptake was higher in the lung and liver for the [^{89}Zr] Zr-DFO-CNC-Cy5 group (Supplementary Fig. S5b). The differences in tumor and bone persisted until 48 h (Supplementary Fig. S5c), suggesting that the accumulation of radioactivity seen in the [^{89}Zr] Zr-DFO-CNC-Cy5 can be at least partially attributed to zirconium-89 released from the CNC construct *in vivo*. This was further corroborated by the lack of significant differences in the tumor-to-blood ratio for either group at any of the time points (Supplementary Fig. S5d), illustrating that the radioactive species that localizes to the tumor after administration of the ^{89}Zr-labeled CNC behaves in part analogously to [^{89}Zr]Zr-oxalate, although the travel of the ^{89}Zr-radioactivity in the blood as intact CNC taken up by

circulating monocytes could not be ruled out. In order to investigate this, we further fractionated the whole blood collected by cardiac puncture at 4 h after an intravenous injection of either [^{89}Zr]Zr-DFO-CNC-Cy5 nanoparticles or [^{89}Zr]Zr-oxalate using density gradient centrifugation to plasma, monocytes and erythrocytes and measured the radioactivity of each fraction by gamma counting (Supplementary Fig. S6). The lack of significant differences between the distribution of radioactivity to the various blood components between the groups further illustrates that the remaining radioactive species in circulation arises from released zirconium-89 *in vivo* for animals dosed with [^{89}Zr]Zr-DFO-CNC-Cy5.

In order to demonstrate the potential of the multimodal cellulose nanocrystal constructs for fluorescence imaging, tissues from 4T1 tumor-bearing mice intravenously injected with 25 μg of either DFO-CNC-Cy5, NOTA-CNC-Cy5, and unmodified nanocrystals were excised at 24 h p.i. and imaged under epifluorescence illumination on a PerkinElmer IVIS Spectrum *in vivo* imaging system with spectral unmixing from tissue autofluorescence determined from the control tissues of a mouse receiving the unmodified CNC. The fluorescence imaging (Fig. 5) corroborated the results of the biodistribution study, as intense fluorescence was seen in the liver, lung, and spleen for DFO-CNC-Cy5, and primarily in the spleen for NOTA-CNC-Cy5. Slight blood pool fluorescence in the heart and blood was also seen for DFO-CNC-Cy5, in line with the observation of the increased blood half-life for this nanocrystal type. Both the kidneys and urine (data not shown) were void of the fluorescent signal. The fluorescence imaging study also revealed that the amount of Cy5 conjugated to the NOTA-modified CNC was likely not sufficient to permit optical imaging and needs to be optimized for subsequent studies.

Tissue samples from the optical imaging study were also processed for cryosections for fluorescence microscopy and for paraffin sections for immunohistochemistry with amplification of the Cy5 signal with a mouse monoclonal α-Cy5 antibody. As expected, the signal from Cy5 alone was not enough to permit visualization of nanocrystal uptake in fluorescence microscopy, and only scattered CNC aggregates were seen in the liver and spleen of animals injected with DFO-CNC-Cy5 and NOTA-CNC-Cy5 (Supplementary Fig. S7a–d). Immunohistochemistry with a mouse monoclonal anti-Cy5-antibody of selected tissues from an animal injected with DFO-CNC-Cy5 showed amplification of the signal in the liver, lung, and spleen (Fig. 6), the principal tissues of CNC accumulation *in vivo.* The specificity of the anti-Cy5 DAB staining was corroborated with both a non-specific IgG, and the staining of a positive control tissue, a HER2-positive human ductal adenocarcinoma BT-474 xenograft from an outbred nude mouse injected intravenously with Cy5-labeled trastuzumab (Herceptin), a HER2-targeting monoclonal antibody.

Hematoxylin–Eosin (H&E) staining of the tissues (Supplementary Fig. S8) showed no gross histopathological changes elicited by either unmodified CNC, DFO-CNC-Cy5, or NOTA-CNC-Cy5 at the dose used at 24 h p.i. Cellulose nanocrystals have shown no acute toxicity in a previous study after systemic delivery of 4.2 μg of CNC [29], but as with any engineered nanomaterial, the material properties will have a profound impact on its biocompatibility and toxicity *in vivo* and need to be evaluated rigorously at therapeutically relevant dosages

before use for carrier-mediated drug delivery. Furthermore, the degradation and tolerance of accumulated CNC in tissues needs to be determined on a longer time scale.

3.3. Multimodal CNC associate primarily with macrophages and Ly-6C^{hi} monocytes in the spleen

Since accumulation of the multimodal CNC after systemic administration to the RES was apparent from the biodistribution data, we decided to further dissect the sequestration of the nanocrystals in the immune cells by flow cytometry. Furthermore, the blood kinetics of [^{89}Zr]Zr-DFO-CNC-Cy5 indicated that the lung might act as a reservoir that initially traps the CNC and gradually releases them to the blood stream. The removal of CNC from the lung is likely to be mediated by uptake into phagocytic cells of the immune system because of their high abundance in the blood and constant presence in the lung, an important physiological barrier to the entry of foreign materials and pathogens into the body [57,58]. For the flow cytometry analysis, single-cell tissue suspensions containing immune cells were collected after intravenous administration of Cy5-labeled DFO- and NOTA-modified CNC from the spleen and the orthotopic 4T1-tdTomato tumor (expressing the fluorescent protein to help identify the tumor cells). Different immune cells were identified by their distinct surface markers and the Cy5 content in the cells was analyzed using flow cytometry. Flow cytometry quantification from the spleen (Fig. 7a) showed accumulation of DFO-CNC-Cy5 to macrophages, dendritic cells, Ly-6C^{hi} monocytes, and neutrophils, while NOTA-CNC-Cy5 was detected only in minute amounts in macrophages and Ly-6C^{hi} monocytes. In the tumor (Fig. 7b), virtually no nanocrystals of either type were detected in any of the cell types studied. Gating procedures for the identification of the different immune cell populations used for the flow cytometry are given in Supplementary Fig. S9a–b. The overall low percentage of Cy5-positive cells in both tissues is likely a result of the fact that only a small fraction of the 50-microgram injected dose accumulated to the spleen and tumor at 2 h p.i., lowering considerably the signal for Cy5. Additionally, the amount of Cy5 conjugated to the CNC might not be enough to permit efficient detection at low concentrations of the nanomaterial.

The results from the spleen indicate that CNC are rapidly internalized by phagocytic cells, with possible inflammatory activation [58,59]. The macrophages and Ly-6C^{hi} monocytes are likely from the splenic reservoir [59,60], although the uptake of nanomaterials to Ly-6C^{hi} monocytes and their patrolling counterparts in the vasculature, the Ly-6C^{low} monocytes, could also occur in the blood and lung capillaries [46,47]. Uptake to macrophages, dendritic cells, and monocytes is a common fate to nanomaterials [61], and has been recently exploited for targeting of tumor-associated macrophages and monocytes for PET imaging [62,63], and for improved chemotherapy and immunotherapy in cancer and cardiovascular disease [64,65]. For the CNC constructs used in this study, a detailed investigation of their sequestration to the leukocyte populations in different compartments of the lung [66], and uptake to circulating monocytes would be in place to evaluate their potential for targeting cells of the immune system. Interestingly, recent reports in mouse models show that the presence of a tumor potentially accelerates nanomaterial clearance through the RES [67], likely through modulation of the ratio of M1 (pro-inflammatory) and M2 (anti-inflammatory) macrophages, and that nanomaterial clearance from circulation is more

pronounced in “Th2-prone” (*i.e.* expressing higher levels of Th2 cytokines driving the transition of the macrophage to the M2 phenotype) mouse strains such as Balb/c [68], which was used in this study as the 4T1 tumor cell line originated in Balb/c mice.

4. Conclusions

The development of new engineered nanomaterials for carriermediated drug delivery necessitates thorough *in vivo* evaluation of the materials for their biodistribution and biocompatibility in clinically relevant animal models. Nanocrystalline cellulose has been already for some time been advertised as a promising nanomaterial for biomedical applications because of its versatile chemistry, facile preparation and high biocompatibility in cell models, but preclinical *in vivo* studies have been scarce. Herein, we have strived to advance the *in vivo* evaluation of CNC materials by developing a multimodality labeling strategy allowing both the non-invasive PET imaging of nanocrystal biodistribution in a mouse model of human stage IV breast cancer, and detection of the nanocrystals *ex vivo* in tissues by fluorescence imaging, microscopy, and flow cytometry. In our study, the non-targeted CNC were rapidly sequestered to the liver and spleen after intravenous administration, indicating immune recognition which was further confirmed by flow cytometry analysis of phagocytic cells. The choice of the radiometal chelator between DFO and NOTA had a profound impact on the biodistribution of the CNC, likely as a result of impacting the material surface charge and subsequent immune recognition of the nanocrystals. Therefore, future studies on the *in vivo* behavior of CNC should be concentrated on improving the nanomaterial stability and circulation half-life under physiological conditions, improving the labeling yields for both radiolabeling and fluorescence labeling to obviate the use of excessively large amounts of radiometal chelator impacting the CNC behavior *in vivo*, and dissecting the immune recognition and biocompatibility of the material to realize the potential of CNC for systemic drug delivery and immune cell targeting. Nevertheless, our studies advance the understanding on the potential pitfalls on the development of CNC multimodal imaging probes in terms of radiometal chelator and conjugation chemistry selection. Out of the two radiolabeled constructs generated in this work, the radiolabeling strategy employing copper-64 and the 1,4,7-triazacyclononane-1,4,7-triacetic acid (NOTA) chelator was superior to zirconium-89 chelation with desferrioxamine B in terms of the specific radioactivity attained and the stability of the radiolabeled construct in terms of both the radiolabel stability and stability of the dispersion in physiological conditions. Our study highlights the importance of the choice of the labeling strategy on the generation of successful imaging probes for engineered nanomaterials for their *in vivo* evaluation.

Supplementary Material

Refer to Web version on PubMed Central for supplementary material.

Acknowledgments

The staff of the Molecular Cytology Core Facility (MCCF) at Memorial Sloan Kettering Cancer Center is thanked for their expert help in the generation of the automated image analysis scripts for MetaMorph, AFM imaging, and with live-cell confocal microscopy. We especially acknowledge M. Brendel for his help with the presentation of the

AFM data. We thank K. Edwards, D.W. Demoin, D. Abdel-Atti, O. Keinänen, and S. Imlimthan for their help with cell culture and animal studies. We gratefully acknowledge funding from the Academy of Finland (decision no. 278056), the University of Helsinki, the NIH Cancer Center Support Grant P30 CA08748–48 (support for the MSKCC Small Animal Imaging, the Molecular Cytology, as well as the Radiochemistry and Molecular Imaging Probe Core Facilities), and the NIH Shared Instrumentation Grant No. 1 S10 RR020892–01 (support for the acquisition of the Focus 120 microPET). The MSKCC Metastasis Research Center is gratefully acknowledged for the Shared Resources Grant that supported the purchase of the IVIS Spectrum instrument.

Abbreviations

AFM	atomic force microscopy
CNC	nanocrystalline cellulose or cellulose nanocrystal(s)
DFO	desferrioxamine B
DAB	3,3′-diaminobenzyl
DAPI	4′,6-diamidino-2-phenylindole
DMSO	dimethylsulfoxide
DTPA	diethylene triamine pentaacetic acid
EDTA	ethylenetriamine tetraacetic acid
NOTA	1,4,7-triazacyclononane-1,4,7-triacetic acid
PET	positron emission tomography
RES	reticuloendothelial system
SPECT	single-photon emission computed tomography

References

[1]. Sun T, Zhang YS, Pang B, Hyun DC, Yang M, Xia Y. Engineered nanoparticles for drug delivery in cancer therapy. Angew Chem Int Ed 2014;53:12320–64.

[2]. Wicki A, Witzigmann D, Balasubramanian V, Huwyler J. Nanomedicine in cancer therapy: challenges, opportunities, and clinical applications. J Control Release 2015;200:138–57. [PubMed: 25545217]

[3]. Gharpure KM, Wu SY, Li C, Lopez-Berestein G, Sood AK. Nanotechnology: future of oncotherapy. Clin Cancer Res 2015;21:3121–30. [PubMed: 26180057]

[4]. Cho K, Wang X, Nie S, Chen Z, Shin DM. Therapeutic nanoparticles for drug delivery in cancer. Clin Cancer Res 2008;14:1310–6. [PubMed: 18316549]

[5]. Wilhelm S, Tavares AJ, Dai Q, Ohta S, Audet J, Dvorak HF, et al. Analysis of nanoparticle delivery to tumours. Nat Rev Mater 2016;1:16014.

[6]. De Souza R, Spence T, Huang H, Allen C. Preclinical imaging and translational animal models of cancer for accelerated clinical implementation of nanotechnologies and macromolecular agents. J Control Release 2015;219:313–30. [PubMed: 26409122]

[7]. Louie A Multimodality imaging probes: design and challenges. Chem Rev 2010;110: 3146–95. [PubMed: 20225900]

[8]. Zeglis BM, Davis CB, Abdel-Atti D, Carlin SD, Chen A, Aggeler R, et al. Chemoenzymatic strategy for the synthesis of site-specifically labeled immunoconjugates for multimodal PET and optical imaging. Bioconjug Chem 2014;25:2123–8. [PubMed: 25418333]

[9]. Habibi Y, Lucia LA, Rojas OJ. Cellulose nanocrystals: chemistry, self-assembly, and applications. Chem Rev 2010;110:3479–500. [PubMed: 20201500]

[10]. Bondeson D, Mathew A, Oksman K. Optimization of the isolation of nanocrystals from microcrystalline cellulose by acid hydrolysis. Cellulose 2006;13:171–80.

[11]. Elazzouzi-Hafraoui S, Nishiyama Y, Putaux J-L, Heux L, Dubreuil F, Rochas C. The shape and size distribution of crystalline nanoparticles prepared by acid hydrolysis of native cellulose. Biomacromolecules 2008;9:57–65. [PubMed: 18052127]

[12]. Sacui IA, Nieuwendaal RC, Burnett DJ, Stranick SJ, Jorfi M, Weder C, et al. Comparison of the properties of cellulose nanocrystals and cellulose nanofibrils isolated from bacteria, tunicate, and wood processed using acid, enzymatic, mechanical, and oxidative methods. ACS Appl Mater Interfaces 2014;6:6127–38. [PubMed: 24746103]

[13]. Moon RJ, Martini A, Nairn J, Simonsen J, Youngblood J. Cellulose nanomaterials review: structure, properties and nanocomposites. Chem Soc Rev 2011;40:3941–94. [PubMed: 21566801]

[14]. Jackson JK, Letchford K, Wasserman BZ, Ye L, Hamad WY, Burt HM. The use of nanocrystalline cellulose for the binding and controlled release of drugs. Int J Nanomedicine 2011;6:321–30. [PubMed: 21383857]

[15]. Lam E, Male KB, Chong JH, Leung ACW, Luong JHT. Applications of functionalized and nanoparticle-modified nanocrystalline cellulose. Trends Biotechnol 2012;30: 283–90. [PubMed: 22405283]

[16]. Valo H, Arola S, Laaksonen P, Torkkeli M, Peltonen L, Linder MB, et al. Drug release from nanoparticles embedded in four different nanofibrillar cellulose aerogels. Eur J Pharm Sci 2013;50:69–77. [PubMed: 23500041]

[17]. Kolakovic R, Peltonen L, Laukkanen A, Hirvonen J, Laaksonen T. Nanofibrillar cellulose films for controlled drug delivery. Eur J Pharm Biopharm 2012;82:308–15. [PubMed: 22750440]

[18]. Moritz S, Wiegand C, Wesarg F, Hessler N, Müller FA, Kralisch D, et al. Active wound dressings based on bacterial nanocellulose as drug delivery system for octenidine. Int J Pharm 2014;471:45–55. [PubMed: 24792978]

[19]. Czapar AE, Zheng Y-R, Riddell IA, Shukla S, Awuah SG, Lippard SJ, et al. Tobacco mosaic virus delivery of phenanthriplatin for cancer therapy. ACS Nano 2016;10: 4119–26. [PubMed: 26982250]

[20]. Bhirde AA, Patel V, Gavard J, Zhang G, Sousa AA, Masedunskas A, et al. Targeted killing of cancer cells in vivo and in vitro with EGF-directed carbon nanotube-based drug delivery. ACS Nano 2009;3:307–16. [PubMed: 19236065]

[21]. Liu Z, Cai W, He L, Nakayama N, Chen K, Sun X, et al. In vivo biodistribution and highly efficient tumour targeting of carbon nanotubes in mice. Nat Nanotechnol 2007;2:47–52. [PubMed: 18654207]

[22]. Chauhan VP, Popović Z, Chen O, Cui J, Fukumura D, Bawendi MG, et al. Fluorescent nanorods and nanospheres for real-time in vivo probing of nanoparticle shape-dependent tumor penetration. Angew Chem Int Ed 2011;50:11417–20.

[23]. Chariou PL, Lee KL, Pokorski JK, Saidel GM, Steinmetz NF. Diffusion and uptake of tobacco mosaic virus as therapeutic carrier in tumor tissue: effect of nanoparticle aspect ratio. J Phys Chem B 2016;120:6120–9. [PubMed: 27045770]

[24]. Catalán J, Ilves M, Järventaus H, Hannukainen K-S, Kontturi E, Vanhala E, et al. Genotoxic and immunotoxic effects of cellulose nanocrystals in vitro. Environ Mol Mutagen 2015;56:171–82. [PubMed: 25257801]

[25]. de Lima R, Feitosa LO, Maruyama CR, Barga MA, Yamawaki PC, Vieira IJ, et al. Evaluation of the genotoxicity of cellulose nanofibers. Int J Nanomedicine 2012;7: 3555–65. [PubMed: 22848179]

[26]. Lou Y-R, Kanninen L, Kuisma T, Niklander J, Noon LA, Burks D, et al. The use of nanofibrillar cellulose hydrogel as a flexible three-dimensional model to culture human pluripotent stem cells. Stem Cells Dev 2014;23:380–92. [PubMed: 24188453]

[27]. Mertaniemi H, Escobedo-Lucea C, Sanz-Garcia A, Gandía C, Mäkitie A, Partanen J, et al. Human stem cell decorated nanocellulose threads for biomedical applications. Biomaterials 2016;82:208–20. [PubMed: 26763735]

[28]. Harper BJ, Clendaniel A, Sinche F, Way D, Hughes M, Schardt J, et al. Impacts of chemical modification on the toxicity of diverse nanocellulose materials to developing zebrafish. Cellulose 2016;23:1763–75. [PubMed: 27468180]

[29]. Colombo L, Zoia L, Violatto MB, Previdi S, Talamini L, Sitia L, et al. Organ distribution and bone tropism of cellulose nanocrystals in living mice. Biomacromolecules 2015; 16:2862–71. [PubMed: 26226200]

[30]. Mahmoud KA, Mena JA, Male KB, Hrapovic S, Kamen A, Luong JHT. Effect of surface charge on the cellular uptake and cytotoxicity of fluorescent labeled cellulose nanocrystals. ACS Appl Mater Interfaces 2010;2:2924–32. [PubMed: 20919683]

[31]. Dong S, Roman M. Fluorescently labeled cellulose nanocrystals for bioimaging applications. J Am Chem Soc 2007;129:13810–1. [PubMed: 17949004]

[32]. Holland JP, Sheh Y, Lewis JS. Standardized methods for the production of high specific-activity zirconium-89. Nucl Med Biol 2009;36:729–39. [PubMed: 19720285]

[33]. Zoppe JO, Ruottinen V, Ruotsalainen J, Rönkkö S, Johansson L-S, Hinkkanen A, et al. Synthesis of cellulose nanocrystals carrying tyrosine sulfate mimetic ligands and inhibition of alphavirus infection. Biomacromolecules 2014;15:1534–42. [PubMed: 24628489]

[34]. Isogai A, Saito T, Fukuzumi H. TEMPO-oxidized cellulose nanofibers. Nanoscale 2011;3:71–85. [PubMed: 20957280]

[35]. Eyley S, Thielemans W. Surface modification of cellulose nanocrystals. Nanoscale 2014;6:7764–79. [PubMed: 24937092]

[36]. Imlimthan S, Otaru S, Keinänen O, Correia A, Lintinen K, Santos HA, et al. Radiolabeled molecular imaging probes for the in vivo evaluation of cellulose nanocrystals for biomedical applications. Biomacromolecules 2019;20:674–83. [PubMed: 30380842]

[37]. Lin N, Huang J, Dufresne A. Preparation, properties and applications of polysaccharide nanocrystals in advanced functional nanomaterials: a review. Nanoscale 2012; 4:3274–94. [PubMed: 22565323]

[38]. Karimi Shervedani R, Akrami Z, Sabzyan H. Nanostructure molecular assemblies constructed based on ex-situ and in-situ layer-by-layer ferrioxamation characterized by electrochemical and scanning tunneling microscopy methods. J Phys Chem C 2011;115:8042–55.

[39]. Serrano Figueroa LO, Pitts B, Uchida M, Richards AM. Vesicle self-assembly of amphiphilic siderophores produced by bacterial isolates from soap Lake, Washington. Can J Chem 2015;94:35–43.

[40]. Sarparanta M, Bimbo LM, Rytkönen J, Mäkilä E, Laaksonen TJ, Laaksonen P, et al. Intravenous delivery of hydrophobin-functionalized porous silicon nanoparticles: stability, plasma protein adsorption and biodistribution. Mol Pharm 2012;9:654–63. [PubMed: 22277076]

[41]. Oh N, Park J-H. Endocytosis and exocytosis of nanoparticles in mammalian cells. Int J Nanomedicine 2014;9:51–63. [PubMed: 24872703]

[42]. Saino E, Focarete ML, Gualandi C, Emanuele E, Cornaglia AI, Imbriani M, et al. Effect of electrospun fiber diameter and alignment on macrophage activation and secretion of proinflammatory cytokines and chemokines. Biomacromolecules 2011;12: 1900–11. [PubMed: 21417396]

[43]. Allegri M, Bianchi MG, Chiu M, Varet J, Costa AL, Ortelli S, et al. Shape-related toxicity of titanium dioxide nanofibres. PLoS One 2016;11:e0151365. [PubMed: 26999274]

[44]. Heppner GH, Miller FR, Malathy Shekhar PV. Nontransgenic models of breast cancer. Breast Cancer Res 2000;2:331–4. [PubMed: 11250725]

[45]. Yokoi K, Tanei T, Godin B, van de Ven AL, Hanibuchi M, Matsunoki A, et al. Serum biomarkers for personalization of nanotherapeutics-based therapy in different tumor and organ microenvironments. Cancer Lett 2014;345:48–55. [PubMed: 24370567]

[46]. Geissmann F, Jung S, Littman DR. Blood monocytes consist of two principal subsets with distinct migratory properties. Immunity 2003;19:71–82. [PubMed: 12871640]

[47]. Tang J, Baxter S, Menon A, Alaarg A, Sanchez-Gaytan BL, Fay F, et al. Immune cell screening of a nanoparticle library improves atherosclerosis therapy. Proc Natl Acad Sci U S A 2016;113 (E6731-E40).

[48]. Monopoli MP, Walczyk D, Campbell A, Elia G, Lynch I, Baldelli Bombelli F, et al. Physical–chemical aspects of protein corona: relevance to in vitro and in vivo biological impacts of nanoparticles. J Am Chem Soc 2011;133:2525–34. [PubMed: 21288025]

[49]. Dobrovolskaia MA, Aggarwal P, Hall JB, McNeil SE. Preclinical studies to understand nanoparticle interaction with the immune system and its potential effects on nanoparticle biodistribution. Mol Pharm 2008;5:487–95. [PubMed: 18510338]

[50]. Aggarwal P, Hall JB, McLeland CB, Dobrovolskaia MA, McNeil SE. Nanoparticle interaction with plasma proteins as it relates to particle biodistribution, biocompatibility and therapeutic efficacy. Adv Drug Deliv Rev 2009;61:428–37. [PubMed: 19376175]

[51]. Pivkin IV, Peng Z, Karniadakis GE, Buffet PA, Dao M, Suresh S. Biomechanics of red blood cells in human spleen and consequences for physiology and disease. Proc Natl Acad Sci U S A 2016;113:7804–9. [PubMed: 27354532]

[52]. Holland JP, Divilov V, Bander NH, Smith-Jones PM, Larson SM, Lewis JS. ^{89}Zr-DFO-J591 for ImmunoPET of prostate-specific membrane antigen expression in vivo. J Nucl Med 2010;51:1293–300. [PubMed: 20660376]

[53]. Vugts DJ, Klaver C, Sewing C, Poot AJ, Adamzek K, Huegli S, et al. Comparison of the octadentate bifunctional chelator DFO*-pPhe-NCS and the clinically used hexadentate bifunctional chelator DFO-pPhe-NCS for ^{89}Zr-immuno-PET. Eur J Nucl Med Mol Imaging 2017;44:286–95. [PubMed: 27573793]

[54]. Deri MA, Ponnala S, Kozlowski P, Burton-Pye BP, Cicek HT, Hu C, et al. p-SCN-Bn-HOPO: a superior bifunctional chelator for ^{89}Zr ImmunoPET. Bioconjug Chem 2015;26:2579–91. [PubMed: 26550847]

[55]. Ma MT, Meszaros LK, Paterson BM, Berry DJ, Cooper MS, Ma Y, et al. Tripodal tris (hydroxypyridinone) ligands for immunoconjugate PET imaging with 89Zr4+: comparison with desferrioxamine-B. Dalton Trans 2015;44:4884–900. [PubMed: 25351250]

[56]. Severin GW, Jørgensen JT, Wiehr S, Rolle A-M, Hansen AE, Maurer A, et al. The impact of weakly bound 89Zr on preclinical studies: non-specific accumulation in solid tumors and aspergillus infection. Nucl Med Biol 2015;42:360–8. [PubMed: 25583221]

[57]. Kopf M, Schneider C, Nobs SP. The development and function of lung-resident macrophages and dendritic cells. Nat Immunol 2015;16:36–44. [PubMed: 25521683]

[58]. Lebre F, Hearnden CH, Lavelle EC. Modulation of immune responses by particulate materials. Adv Mater 2016;28:5525–41. [PubMed: 27167228]

[59]. Shi C, Pamer EG. Monocyte recruitment during infection and inflammation. Nat Rev Immunol 2011;11:762–74. [PubMed: 21984070]

[60]. Davies LC, Jenkins SJ, Allen JE, Taylor PR. Tissue-resident macrophages. Nat Immunol 2013;14:986–95. [PubMed: 24048120]

[61]. Owens DE III, Peppas NA. Opsonization, biodistribution, and pharmacokinetics of polymeric nanoparticles. Int J Pharm 2006;307:93–102. [PubMed: 16303268]

[62]. Pérez-Medina C, Tang J, Abdel-Atti D, Hogstad B, Merad M, Fisher EA, et al. PET imaging of tumor-associated macrophages with ^{89}Zr-labeled high-density lipoprotein nanoparticles. J Nucl Med 2015;56:1272–7. [PubMed: 26112022]

[63]. Normandin MD, Yuan H, Wilks MQ, Chen HH, Kinsella JM, Cho H, et al. Heat-induced radiolabeling of nanoparticles for monocyte tracking by PET. Angew Chem Int Ed 2015;54:13002–6.

[64]. Lameijer MA, Tang J, Nahrendorf M, Beelen RHJ, Mulder WJM. Monocytes and macrophages as nanomedicinal targets for improved diagnosis and treatment of disease. Expert Rev Mol Diagn 2013;13:567–80. [PubMed: 23895127]

[65]. Lizotte PH, Wen AM, Sheen MR, Fields J, Rojanasopondist P, Steinmetz NF, et al. In situ vaccination with cowpea mosaic virus nanoparticles suppresses metastatic cancer. Nat Nanotechnol 2016;11:295–303. [PubMed: 26689376]

[66]. Patel BV, Tatham KC, Wilson MR, Dea KP, Takata M. In vivo compartmental analysis of leukocytes in mouse lungs. Am J Physiol 2015;309 (L639-L52).

[67]. Kai MP, Brighton HE, Fromen CA, Shen TW, Luft JC, Luft YE, et al. Tumor presence induces global immune changes and enhances nanoparticle clearance. ACS Nano 2016;10:861–70. [PubMed: 26592524]

[68]. Jones SW, Roberts RA, Robbins GR, Perry JL, Kai MP, Chen K, et al. Nanoparticle clearance is governed by Th1/Th2 immunity and strain background. J Clin Invest 2013; 123:3061–73. [PubMed: 23778144]

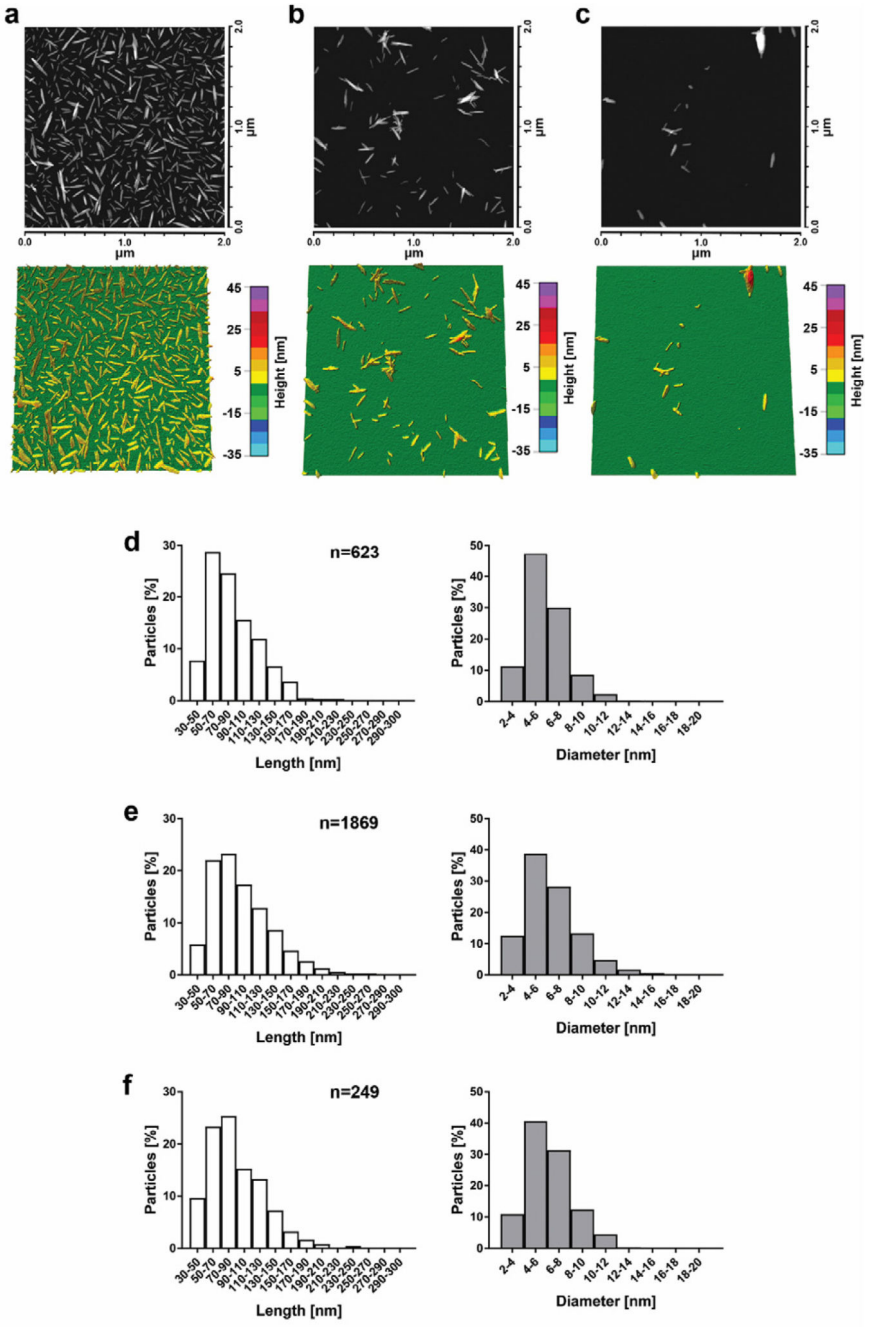

Fig. 1.

Representative AFM images and 3D height maps for unmodified CNC (a), NOTA-CNC-Cy5 (b), and DFO-CNC-Cy5 (c), with corresponding length and diameter distributions derived from the morphometric analysis of >100 individual nanocrystals for unmodified CNC (d), NOTA-CNC-Cy5 (e), and DFO-CNC-Cy5 (f). Columns represent the percentage of particles analyzed falling within the given length and diameter range; n denotes the number of nanocrystals analyzed. A considerably smaller number of nanocrystals could be analyzed for DFO-CNC-Cy5 because of prominent aggregation of the sample upon application on the substrate.

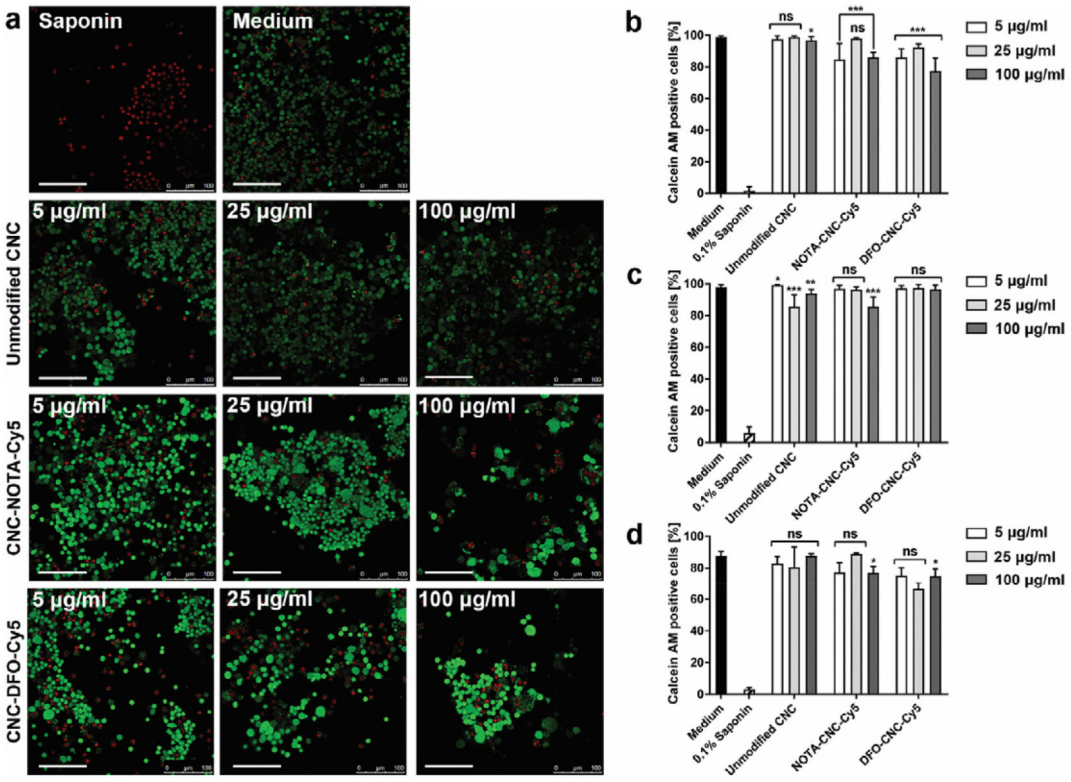

Fig. 2.

a) Representative confocal microscopy images of RAW 264.7 macrophages incubated with different concentrations of unmodified CNC, NOTA-CNC-Cy5, and DFO-CNC-Cy5 for 96 h. Nuclei of dead cells stain red with EthD-1 after loss off cell membrane integrity, while live cells stain green with Calcein AM due to intracellular esterase activity. Medium and 0.1% saponin are used as controls for live and dead cells, respectively. Scale bar 100 µm. Quantification of the proportion of Calcein AM–positive cells at 6 h (b), 24 h (c), and 96 h (d) of incubation with different concentrations of unmodified and modified cellulose nanocrystals. Columns denote mean ± SD of $n = 6.5 \pm 0.5$ (mean ± SEM) analyzed images per time point. Statistical significance of the difference against the positive control was determined by unpaired Mann-Whitney U test with *$p < 0.05$, **$p < 0.01$, and ***$p < 0.001$; ns, not significant.

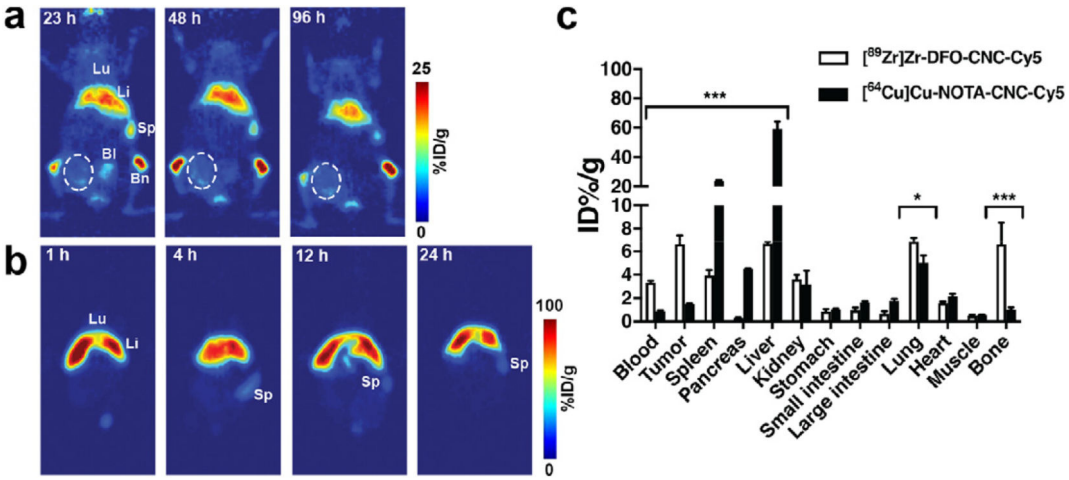

Fig. 3.

a) Serial PET imaging of the same animal bearing single orthotopic 4T1 mammary fat pad allograft after intravenous administration of 3.7 MBq (60 μg) of [^{89}Zr]Zr-DFO-CNC-Cy5 shows accumulation of the nanocrystals in the liver, spleen, and bone. The tumor area (circled) shows only slight radioactive signal on the perimeter of the tumor. b) Serial PET imaging of a single mouse after intravenous administration of 7.4 MBq (60 μg) of [^{64}Cu]Cu-NOTA-CNC-Cy5 shows rapid accumulation of the tracer in the liver, preventing delineation of the tumor in the image. Lu, lung; Li, liver; Sp, spleen; Bl, bladder; Bm, bone with marrow. PET images were acquired under isoflurane anesthesia on a Focus 120 Micro-PET small animal PET scanner with the imaging protocol set to register a minimum of 20 million coincidence events. c) *Ex vivo* biodistribution of [^{89}Zr]Zr-DFO-CNC-Cy5 and [^{64}Cu]Cu-NOTA-CNC-Cy5 at 24 h p.i. shows significant differences in the biodistribution of the two materials. Columns denote mean ± SD of $n = 3$. Statistical analysis was carried out with an unpaired *t*-test with the two-stage step-up method of Benjamin, Krieger and Yekutieli with the false discovery rate set to Q = 10%; *$p < 0.05$, **$p < 0.01$, and ***$p < 0.001$.

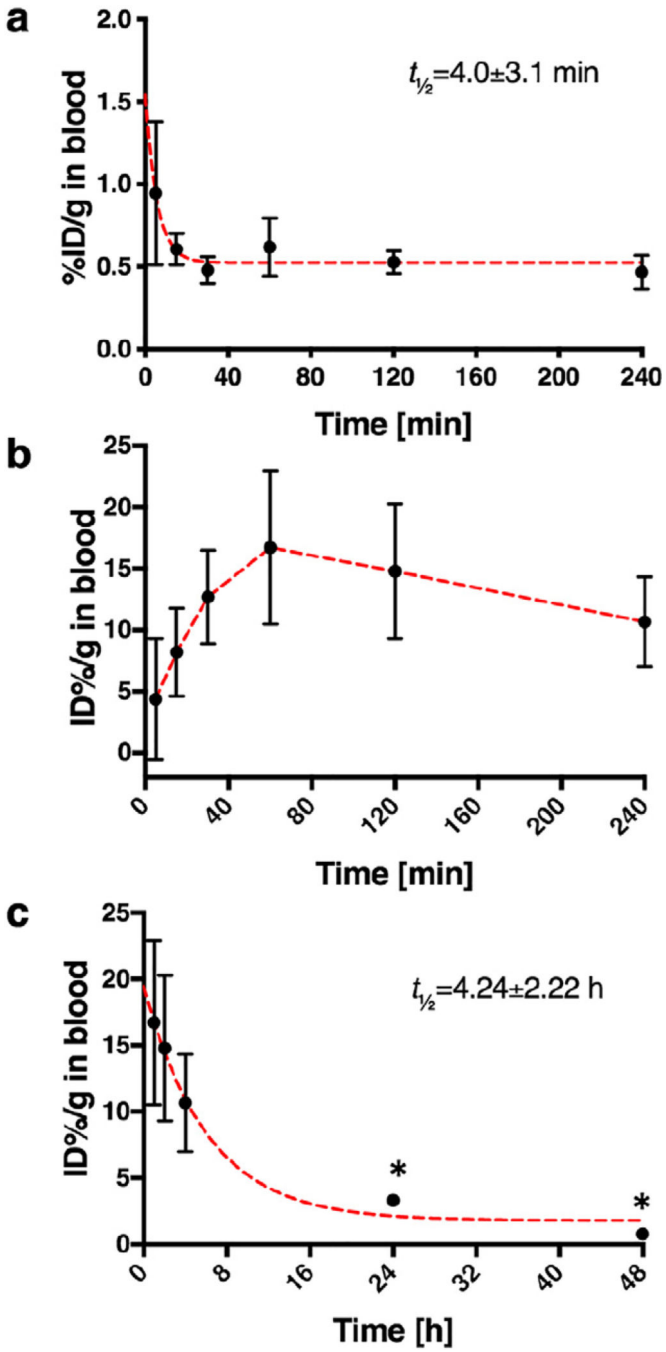

Fig. 4.

a) Blood half-life curve for [^{64}Cu]Cu-NOTA-CNC-Cy5, markers represent mean ± SD of five samples per time point with fitted exponential one-phase decay (red dashed line) to determine the half-life, R^2 = 0.3974; b) Early time points in the blood sampling for [^{89}Zr]Zr-CNC-DFO-Cy5 showed the slow release of radioactivity from an unknown reservoir, presumably the lung, to the circulation after 60 min. Markers represent mean ± SD of five samples, the dashed line in red is guide for the eye only. c) In order to determine the blood half-life of [^{89}Zr]Zr-CNC-DFO-Cy5, the data for 60–240 min in b) was supplemented with

blood values from the biodistribution study at 24 and 48 h (*; $n = 3$ per time point, markers represent mean ± SD). Red dashed line shows fitted exponential one-phase decay with $R^2 = 0.6225$.

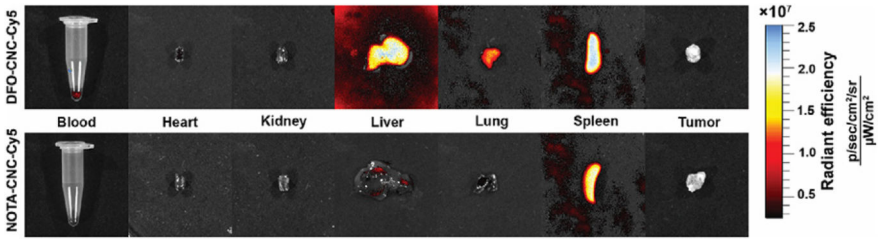

Fig. 5.

Ex vivo fluorescence imaging of selected tissues from animals injected with 25 μg of either DFO-CNC-Cy5 or NOTA-CNC-Cy5 at 24 h p.i. corroborated the biodistribution pattern seen with the radiolabeled cellulose nanocrystals. For DFO-CNC-Cy5, intense fluorescence was seen in the RES, the liver and the spleen, with residual signal in the lung and the blood pool. For NOTA-CNC-Cy5, the bulk of the signal was seen in the spleen, with slight fluorescence present in the liver and lung.

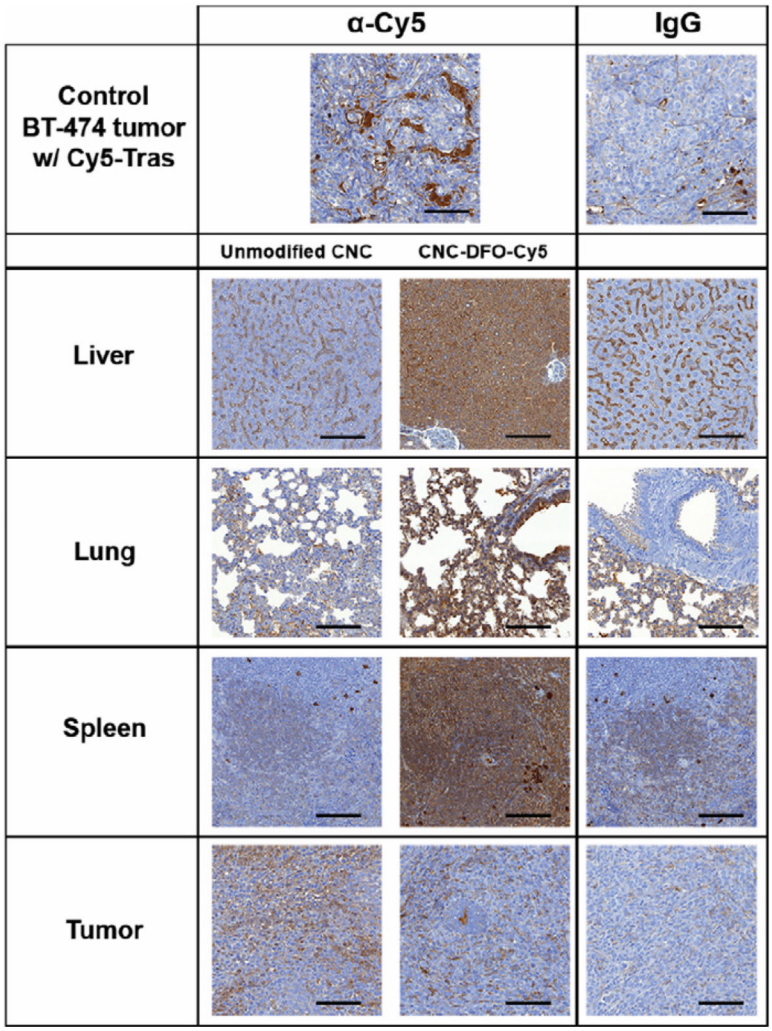

Fig. 6.

DAB immunohistochemistry and Cy5 signal amplification with an anti-Cy5 antibody in paraffin sections of tissues from 4T1 tumor-bearing mice injected intravenously with 25 μg of either unmodified CNC, or DFO-CNC-Cy5. A HER2-positive human ductal adenocarcinoma BT-474 xenograft grown in a nu/nu mouse injected with Cy5-labeled HER2-targeting monoclonal antibody trastuzumab was used as a positive control. Magnification 10×, scale bar 100 μm. Intense DAB staining in the liver, lung, and spleen of the animal receiving DFO-CNC-Cy5 further supports the presence of Cy5-labeled CNC in these organs.

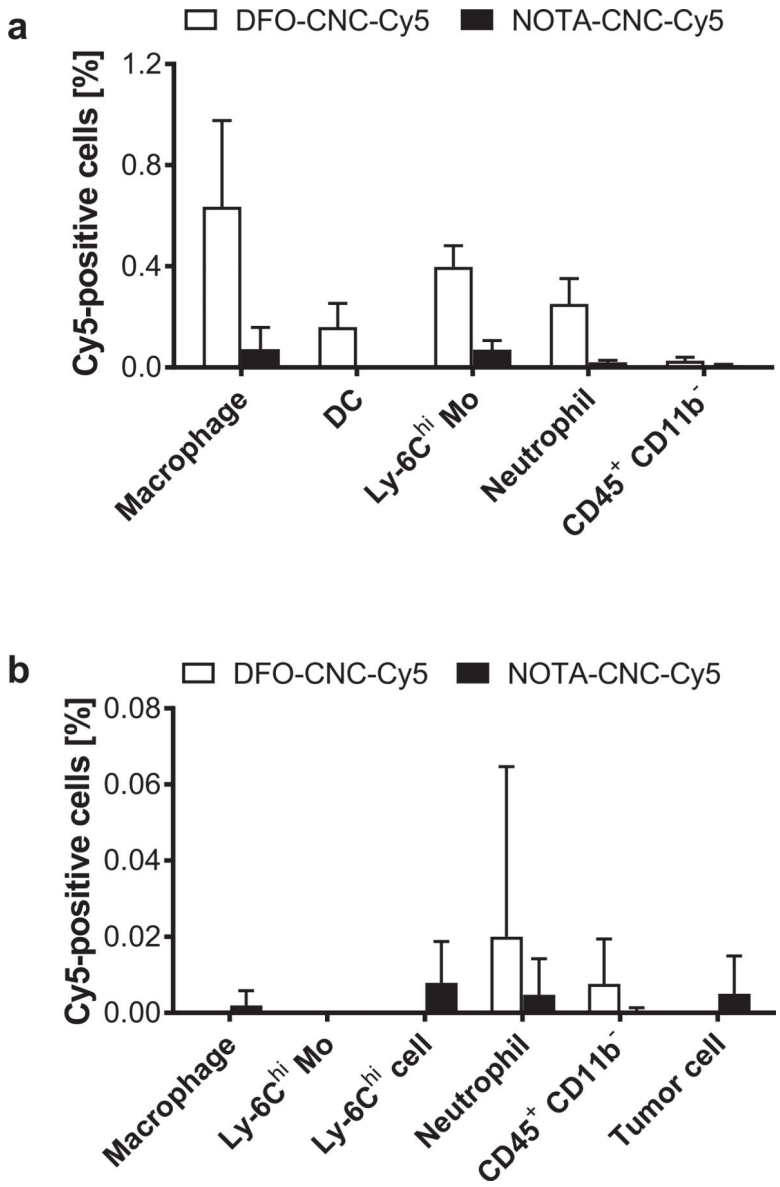

Fig. 7.

a) Sequestration of Cy5-labeled DFO- and NOTA-modified cellulose nanocrystals to immune cells in the mouse spleen 120 min after a single intravenous administration of 50 μg of the nanocrystals shows uptake of DFO-CNC-Cy5 to macrophages, dendritic cells (DC), Ly-6C^{hi} monocytes (Mo) and neutrophils, with only very low numbers of Cy5-positive macrophages and Ly-6C^{hi} monocytes detected for NOTA-CNC-Cy5. b) Negligible uptake of either DFO-CNC-Cy5 or NOTA-CNC-Cy5 is seen in the orthotopic 4T1-tdTomato tumor confirming that the nanocrystals do not reach the tumor by passive targeting. Columns denote mean ± SEM of $n = 5$ for DFO-CNC-Cy5 and $n = 4$ for NOTA-CNC-Cy5.

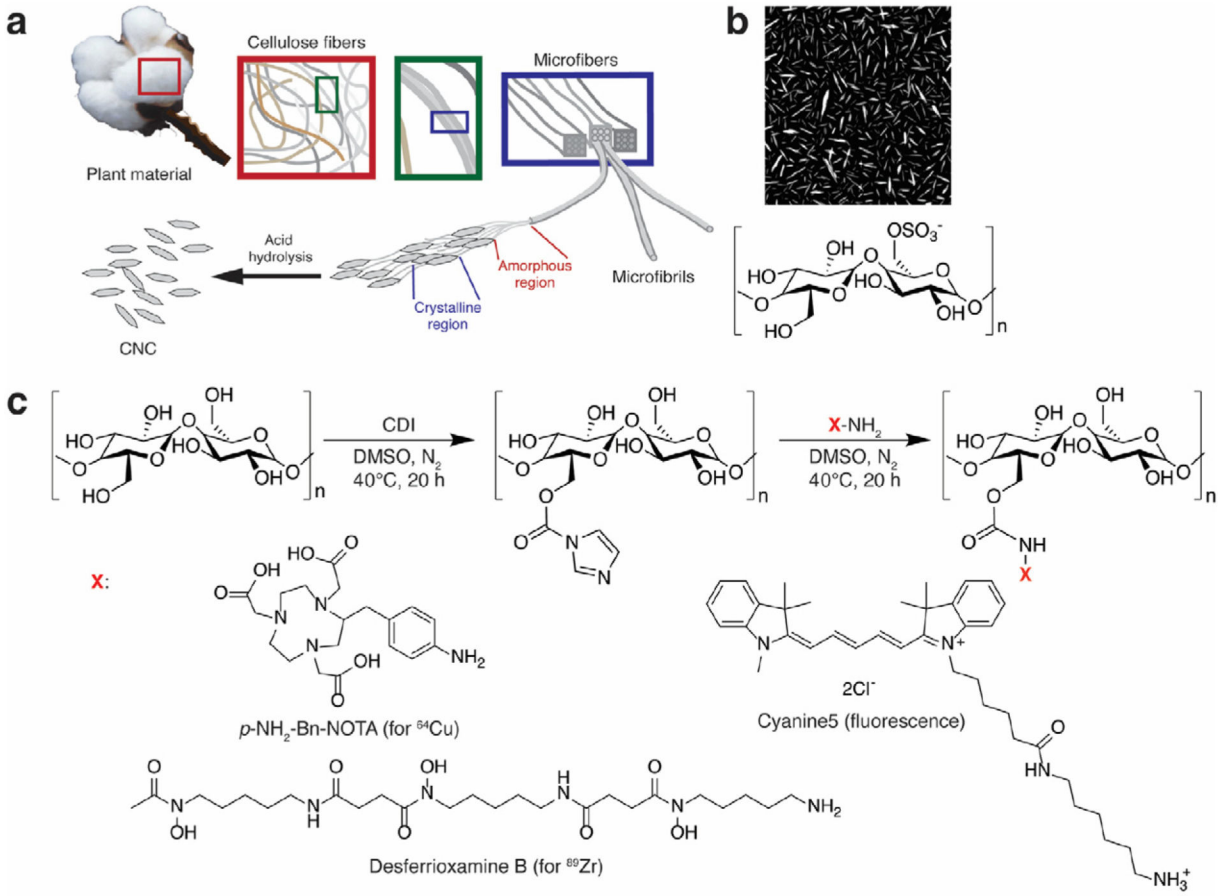

Scheme 1.

a) Schematic representation of CNC preparation from plant cellulose by selective acid hydrolysis of amorphous regions. b) AFM image of as-hydrolyzed CNC with residual sulfate ester groups. c) CNC activation with 1,1′-carbonyldiimidazole (CDI) followed by conjugation of amine-functionalized radiometal chelators p-NH_2-Bn-NOTA (for copper-64), desferrioxamine B (DFO, for zirconium-89), and the Cyanine5 (Cy5) fluorophore.

Table 1

Characterization data for the cellulose nanocrystals developed in this study.

Nanocrystal type	Mean length ± SD [nm][a]	Mean diameter ± SD [nm][a]	Zeta potential [mV]
Unmodified CNC	60.76 ± 24.63	4.37 ± 1.74	−41.6
NOTA-CNC-Cy5	87.62 ± 32.90	5.94 ± 1.79	−20.8
DFO-CNC-Cy5	89.74 ± 35.10	6.25 ± 1.92	−14.7

[a]Data derived from AFM.